Chinese Chemical Letters 37 (2026) 110702

Contents lists available at ScienceDirect

Chinese Chemical Letters

journal homepage: www.elsevier.com/locate/cclet

Hybrid organic-inorganic modification on tunnel-structured α-MnO_2 for high-performance aqueous zinc-ion battery

Mengdan Tian, Chuanzheng Zhu, Kun Luo*

School of Materials Science and Engineering, Tianjin University of Technology, Tianjin 300384, China

ARTICLE INFO

Article history:
Received 10 September 2024
Revised 25 November 2024
Accepted 29 November 2024
Available online 29 November 2024

Keywords:
Aqueous zinc-ion batteries
Hybrid organic-inorganic modification
MnO_2 electrode material
Synergistic effect
Stability

ABSTRACT

Rechargeable aqueous zinc-ion batteries (AZIBs) draw intensive attention due to their high security, low price and the abundant zinc source. However, the electrochemical behaviors of AZIBs are seriously affected by the cathode materials. Mn-based oxide cathodes have been extensively investigated owing to the superior electrochemical performances such as large theoretical capacity and high working voltage. In this work, we rationally design a high-performance cathode material using organic-inorganic co-modification strategy. The inorganic Al^{3+} ions and organic poly-vinylpyrrolidone (PVP) are successfully incorporated into the tunnel α-MnO_2 structure. Structural characterizations and DFT calculations indicates that the Zn^{2+} adsorption energy in the Al^{3+}/PVP co-intercalated tunnel α-MnO_2 is effectively lowered when compared with the original material, facilitating fast ion diffusion and stable Zn^{2+} ion storage. Electrochemical tests indicate that the PVP-Al-MnO_2 electrode exhibits excellent electrochemical performances, a capacity of 306.8 mAh/g at 0.3 A/g and 93.1 % capacity retention over 2000 cycles at 1.0 A/g. In addition, the aqueous PVP-Al-MnO_2||$ZnClO_4$||Zn battery is able to operate properly at low temperature (-45 °C). This work shows an encouraging strategy to the modification of materials for AZIBs and other multivalent ion systems.

© 2025 Published by Elsevier B.V. on behalf of Chinese Chemical Society and Institute of Materia Medica, Chinese Academy of Medical Sciences.

Lithium-ion batteries (LIBs) are broadly utilized in the energy storage market. The uneven distribution of Li source and flammable organic electrolytes bring about high industry cost and safety problems in practical applications [1–6]. The AZIB systems constructed using aqueous electrolytes and Zn metal anode, are viewed as a potential battery system owing to low price, high security, non-flammability, high energy density, and abundant Zn reserves [7–14]. The advancement of AZIBs requires the cathode materials with outstanding electrochemical behaviors (*e.g.*, high energy density and cycling stability) [15].

Mn-based oxide cathode materials have been increasingly explored owing to large theoretical capacity, high working voltage, eco-friendliness, natural abundance and low cost [16–19]. MnO_2 has diverse crystallographic polymorphs (*e.g.*, α-MnO_2 [20], β-MnO_2 [21], δ-MnO_2 [22] and γ-MnO_2 [23]), and is therefore considered as a prominent cathode material. However, the application of MnO_2 cathode still faces many technical problems. Low electronic conductivity seriously limits the energy storage ability of MnO_2 materials [24–26]. Strong Zn^{2+}-MnO_2 columbic interaction leads to a sluggish Zn^{2+} diffusion kinetics in the structure [27,28], which could cause the structural collapse at high Zn^{2+} intercalation condition during the electrochemical reaction of Zn^{2+}/H^+ co-intercalation [29]. Furthermore, MnO_2 can be dissolve into the electrolyte in the electrochemical reactions, which also leads to structural breakdown and capacity attenuation during cycling [30].

To resolve these problems, various methods have been attempted to modify the MnO_2 cathode materials. Metal ion pre-intercalation into MnO_2 materials is able to effectively enhance their electrochemical performances. For example, Chen *et al.* reported that cobalt can be pre-intercalated into α-MnO_2, which effectively enhances the structural stability of MnO_2 and promotes the ion diffusion and zinc ion adsorption upon battery cycling [31]. The pre-intercalation of Bi^{3+} into α-MnO_2 can increase the electrical conductivity, weaken the Zn^{2+}-O^{2-} chemical bond and enhance structural stability [32].

The intercalation of organic molecules into MnO_2 is also proved to enhance the electrochemical performances. For example, the intercalation of organic poly-vinylpyrrolidone (PVP) into the layered δ-MnO_2 can validly improve the electrochemical performances of oxide material, because the C=O groups in PVP can facilitate H^+ ion absorption and transportation [33]. The introduction of poly(4,4'-oxybisbenzenamine) (PODA) into α-MnO_2 can effectively boost ion diffusion and control manganese dissolution, im-

* Corresponding author.
E-mail address: kunluo@email.tjut.edu.cn (K. Luo).

https://doi.org/10.1016/j.cclet.2024.110702
1001-8417/© 2025 Published by Elsevier B.V. on behalf of Chinese Chemical Society and Institute of Materia Medica, Chinese Academy of Medical Sciences.

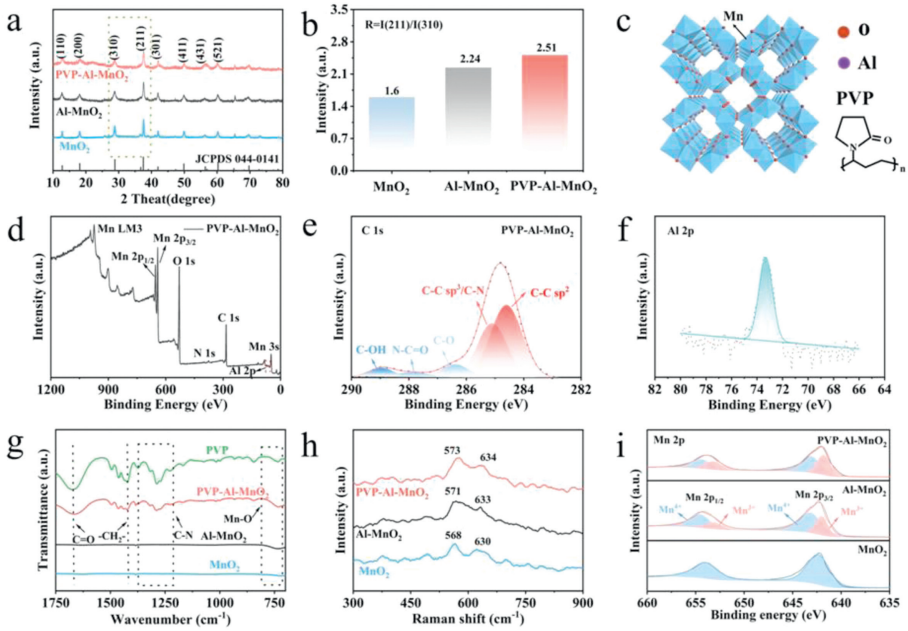


Fig. 1. Structural characterizations of PVP-Al-MnO_2. (a) XRD patterns of pristine α-MnO_2, Al-MnO_2 and PVP-Al-MnO_2. (b) The intensity ratios of (211)/(310) peaks for three samples. (c) The crystal framework of α-MnO_2 with Al ions and PVP intercalation. (d) XPS survey spectra. (e) C 1s XPS result of PVP-Al-MnO_2. (f) Al 2p XPS result of PVP-Al-MnO_2. (g) FTIR spectra of PVP, PVP-Al-MnO_2, Al-MnO_2 and MnO_2. (h) Raman spectra. (i) Mn 2p XPS spectra of three samples.

proving redox dynamics and structural integrity of materials. The PODA chains with C=N groups can give more surface/interface for ion/electron migration and Zn^{2+} storage in the material [34]. The polyaniline (PANI)-reinforced the layered δ-MnO_2 can validly inhibit the H^+/Zn^{2+} insertion and the structural breakdown, which is considered to be beneficial for the long cycling life and high capacity [35].

Recently, the organic-inorganic co-modification strategy has been applied in some vanadate-based oxide materials. The Na^+ and polyaniline co-intercalation into ammonium vanadate (NaNVO-PANI) shows high reversible capacity (610.7 mAh/g) and exceptional cycling stability (98 % after 5000 cycles). The synergistic effect of organic-inorganic co-modification in NaNVO-PANI expands the interlayer spacing, improves the electronic conductivity and lowers zinc ion diffusion barrier [36]. The Zn^{2+} and $C_5H_{14}ON^+$ are successfully inserted into layered V_2O_5. The inherent high conductivity of $C_5H_{14}ON^+$ and the oxygen vacancies created *via* ion pre-intercalation promote the electrical transfer. The synergistic co-inserted method enlarges the layer spacing, boosts the electronic conductivity, gives more active sites for zinc absorption and reinforces the structural stability upon Zn intercalation [37].

In this work, we utilize organic-inorganic co-modification strategy in the tunnel α-MnO_2 structure. The α-MnO_2 is composed by a group of [MnO_6] octahedra with a tunnel 2×2 structure and the channel of ~4.6 Å × 4.6 Å. The structural stability and appropriate channel in α-MnO_2 facilitate fast and reversible insertion and extraction for Zn^{2+} in the electrochemical reactions [31]. The inorganic Al^{3+} ions and organic poly-vinylpyrrolidone (PVP) are successfully incorporated into the α-MnO_2 structure *via* a simple hydrothermal method. The C=O groups in PVP were reported to be able to facilitate cations absorption and transportation, which can catch cations with reduced diffusion barriers and faster proton diffusion [33]. Structural characterizations indicate that the Al^{3+}/PVP co-intercalation results in the deformation of MnO_6 octahedral framework in the tunnel α-MnO_2 structure. DFT calculations displays that the Zn^{2+} adsorption energy in the Al^{3+}/PVP co-intercalated material is effectively lowered when compared with the original α-MnO_2 structure. Electrochemical tests indicate that the PVP-Al-MnO_2 electrode exhibits excellent electrochemical performances, a capacity of 306.8 mAh/g at 0.3 A/g and 93.1 % capacity retention over 2000 cycles at 1.0 A/g. In addition, the aqueous PVP-Al-MnO_2||$ZnClO_4$||Zn battery is able to work properly at low temperature (-45 °C). This work introduces an effective method to modify and optimize the advanced materials for AZIBs.

The α-MnO_2, Al-MnO_2 and PVP-Al-MnO_2 samples were synthesized through a hydrothermal method as depicted in the supporting information. The XRD data were collected in order to get the information on the crystal structures of three samples. All diffraction peaks can correspond to the characteristic peaks of α-MnO_2 (JCPDS No. 044-0141) with tunnel structure (Figs. 1a and c). The peaks at 12.8°, 18.1°, 28.8° and 37.5° were indexed to the (110), (200), (310) and (211) facets, respectively. Previous studies demonstrate that the intercalation of metal atoms into the layered δ-MnO_2 commonly results in the expanded lattice space, displaying on the angle shift of diffraction peaks [38,39]. Nevertheless, there is no obvious angle shift in the Al-intercalated and PVP-Al-intercalated samples (Fig. 1a), which should be attributed to the stable three-dimensional framework of tunnel α-MnO_2 (Fig. 1c). However, the obvious changes of diffraction intensity can be clearly observed on the (211) and (310) peaks. As shown in Fig. 1b, the Al-intercalated ($R = 2.24$) and PVP-Al-intercalated ($R = 2.51$) samples show higher intensity ratios of the characteristic peaks [$R = I(211)/I(310)$] than the pristine α-MnO_2 sample ($R = 1.6$). Similar phenomena were also observed in the 3D tunnel-structured $FeF_3 \cdot 0.33H_2O$ with Nb doping [40,41]. In addition, the intensity of (002) peak in the layered δ-MnO_2 is significantly weakened after the intercalation of PVP into layered structure [33]. Therefore, the intensity variation of (211)/(310) peaks observed in PVP-Al-MnO_2 (Fig. 1b) should be attributed to the distortion of MnO_6 octahedral framework with Al ions and PVP intercalation.

The full survey of XPS was collected in order to determine the chemical composition of PVP-Al-MnO_2 (Fig. 1d), showing the signal peaks of Al 2p, C 1s, N 1s, O 1s, Mn $2p_{1/2}$ and Mn $2p_{3/2}$. Successful insertion of PVP and Al^{3+} ions into α-MnO_2 is evidenced by the existence of N-C=O (Fig. 1e), N (Fig. S1 in Supporting information) and Al (Fig. 1f) as shown in the XPS results, consis-

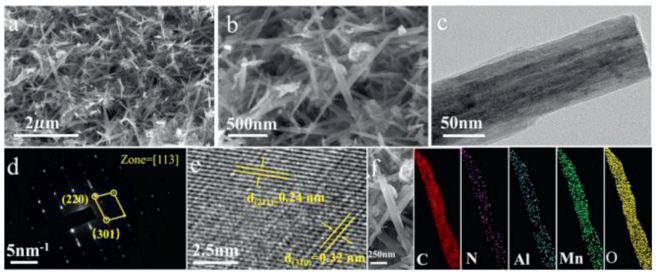


Fig. 2. Morphological information of PVP-Al-MnO_2. (a, b) SEM images of PVP-Al-MnO_2. (c) TEM image. (d) HAADF-SAED pattern. (e) HRTEM image. (f) Element mapping images of PVP-Al-MnO_2.

tent with previous results [33,42,43]. FTIR spectra (Fig. 1g) indicate the typical vibrations of C=O, -CH_2- and C-N groups in PVP-Al-MnO_2. Raman spectra reveal the symmetric Mn-O vibrations for the PVP-Al-MnO_2 (Fig. 1h), which are associated with the bands centered at ~573 and 634 cm^{-1}. The results indicate that the 3D tunnel structure consisting of MnO_6 octahedra is well-maintained after the PVP and Al ions intercalation, and the blue shift observed in PVP-Al-MnO_2 compared with α-MnO_2 should be attributed to the structural distortion of 3D tunnel framework after the PVP and Al ions intercalation, consistent with previous report [44,45]. The Mn 2p spectra of MnO_2, Al-MnO_2 and PVP-Al-MnO_2 were collected in order to determine the Mn valence variation after the chemical modifications (Fig. 1i). The peaks at 654.5 and 643.5 eV are clearly observed in α-MnO_2, matching well to $2p_{1/2}$ and $2p_{3/2}$ signals of Mn^{4+}. The oxidation state of Mn is reduced in PVP-Al-MnO_2. The presence of Jahn-Teller Mn^{3+} cations in PVP-Al-MnO_2 also leads to the structural distortion of 3D tunnel framework, consistent with the observations in XRD patterns (Figs. 1a and b) and Raman spectra (Fig. 1h). Overall, the Al ions and PVP are proved to be successfully incorporated into α-MnO_2 with 3D tunnel structure *via* a simple hydrothermal method.

The morphological information of all the samples was collected using SEM and TEM. PVP-Al-MnO_2, Al-MnO_2 and bare MnO_2 all exhibits nanofibre morphologies (Figs. 2a–c and Fig. S2 in Supporting information). SAED was performed in order to obtain the structural information on PVP-Al-MnO_2, and the result is shown in Fig. 2d. The spots can be well indexed to the typical reflections of tunnel structure along the [113] zone. The lattice spacings of 0.24 nm and 0.32 nm can be seen in HRTEM (Fig. 2e) image, which matches well to the (211) and (310) planes of tetragonal *a*-MnO_2 phase. The elemental mapping images (Fig. 2f) present a uniform distribution of C, N, Al, Mn and O elements, confirming the formation of PVP-Al-MnO_2 material.

The electrochemical behaviors of PVP-Al-MnO_2 were studied in coin batteries with Zn as the negative electrode. The electrochemical performances of PVP-Al-MnO_2 were investigated by charge/discharge in the voltage of 0.8-1.8 V at 0.3 A/g (Fig. 3a). The charge/discharge profiles of MnO_2, Al-MnO_2 and PVP-Al-MnO_2 cathodes in the 1st cycle at 0.3 A/g (Fig. 3a). The PVP-Al-MnO_2 cathode provides a capacity of 306.8 mAh/g, which is higher than the values of Al-MnO_2 (228.7 mAh/g) or MnO_2 (137.3 mAh/g). The EIS was tested to acquire the information on the conductivity of PVP-Al-MnO_2 and MnO_2 (Fig. 3b). The R_{ct} value of PVP-Al-MnO_2 (7.5 Ω) is prominently lower than that of MnO_2 (14.3 Ω), revealing that the PVP-Al-MnO_2 material has faster charge transfer. Figs. 3c and d show the rate capabilities of PVP-Al-MnO_2, Al-MnO_2 (Figs. S3 and S4 in Supporting information) and MnO_2 from 0.3 A/g to 1.5 A/g. PVP-Al-MnO_2 shows the enhanced rate performances when compared with the original α-MnO_2, and delivers reversible capacities of 314.4, 275.5, 250.8, 218.4 and 178.4 mAh/g at 0.3, 0.5, 0.7, 1.0 and 1.5 A/g, respectively. The capacity of PVP-Al-MnO_2 returns to 307.9 mAh/g when the current density is reset to 0.3 A/g, demonstrating a rapid reaction kinetics and extraordinary reversibility upon fast Zn ion insertion/extraction. The cycling performances of PVP-Al-MnO_2 were explored at 0.3 A/g (Fig. 3e and Fig. S5 in Supporting information). The capacity of PVP-Al-MnO_2 is 306.8 mAh/g in the 1st cycle, which is significantly higher than Al-MnO_2 (228.7 mAh/g) and MnO_2 (137.3 mAh/g). The battery shows capacity retention of 99.6 % after 50 cycles and delivers reversible capacities of 300.9, 300.6, 302.9, 304.3 and 305.5 mAh/g at the 10th, 20th, 30th, 40th and 50th cycles (Fig. 3f). The charge/discharge profiles are well maintained during the cycling, demonstrating excellent structural stability of PVP-Al-MnO_2 material upon repetitive Zn^{2+} insertion/extraction. To study the cycling behaviors of PVP-Al-MnO_2, the material was examined at 1.0 A/g (Fig. 3g and Fig. S6 in Supporting information). The PVP-Al-MnO_2 cathode provides an initial capacity of 189.9 mAh/g with the capacity retention of 93.1 % after 2000 cycles. Overall, the high capacity and superior capacity retention of PVP-Al-MnO_2 implies that the kinetics and electrochemical stability of tunnel MnO_2 were effectively improved by the synergistic role of PVP and Al co-doping. As discussed in Fig. 1, the incorporation of PVP and Al into α-MnO_2 leads to the distortion of MnO_6 octahedral framework, which lowers the geometric symmetry of the ligand field and removes the 3d orbital degeneracy of the Mn center. The Jahn-Teller distortion of Mn^{3+} center is effectively inhibited and the cycling steadiness is remarkably enhanced. In addition, low-valence Mn results in a reduction in electrostatic repulsion, thereby effectively enhancing rate performances [46]. The electrochemical behaviors of our PVP-Al-MnO_2 material are also compared with other Mn-based materials (Table S1 in Supporting information and Fig. 3h). For example, the anion-deficient $MnO_{2-\delta}$ cathode shows a capacity of 147 mAh/g with capacity retention of only 78 % after 1000 cycles [47]. The Zn pre-inserted $ZnMn_2O_4$ cathode shows a capacity of 166.6 mAh/g at 1.0 A/g, and the capacity can retain 143.9 mAh/g after 1500 cycles with 86.4 % capacity retention [48]. It is demonstrated that the PVP and Al co-doping in tunnel α-MnO_2 can effectively promote the electrochemical performances and cycling stability.

To obtain the information on the charge storage and kinetic mechanism of PVP-Al-MnO_2, CV tests were applied to detect the energy storage behaviors of PVP-Al-MnO_2 (Fig. 4a). The curve shows 2 pairs of redox peaks clearly, matching well to the reversible insertion/extraction of hydrogen ion and zinc ion in the electrochemical processes as reported previously about the tunnel α-MnO_2 material [49,50]. The peak current (i) and sweep rate (v) can be referred by the formula [51,52]:

$$i = av^b \tag{1}$$

$$\log i = b\log v + \log a \tag{2}$$

where a and b are variants, and the b value is an important parameter to judge the dominant capacity contribution. The b values of the four main peaks are approaching to 1 (0.68, 0.79, 0.77 and 0.89) (Fig. 4b), demonstrating the charge storage behavior of PVP-Al-MnO_2 cathode is controlled by the capacitance process. The contribution of capacitive-like reaction in PVP-Al-MnO_2 cathode accounts for 89.3 % at 1.0 mV/s (Fig. 4c). Additionally, the formula is used to elucidate the particular ratio of 2 various capacity contributions in PVP-Al-MnO_2 cathode [53]:

$$i(\mathrm{V}) = k_1 v = k_2 v^{1/2} \tag{3}$$

i is the current value. k_1 and k_2 denote the capacitive-like and diffusion-control ratio, respectively. The various contribution proportions at different scan rates are shown in Fig. S7 (Supporting information). To summarize capacitive contribution (Fig. S7), the pseudocapacitance contribution is gradually increased from

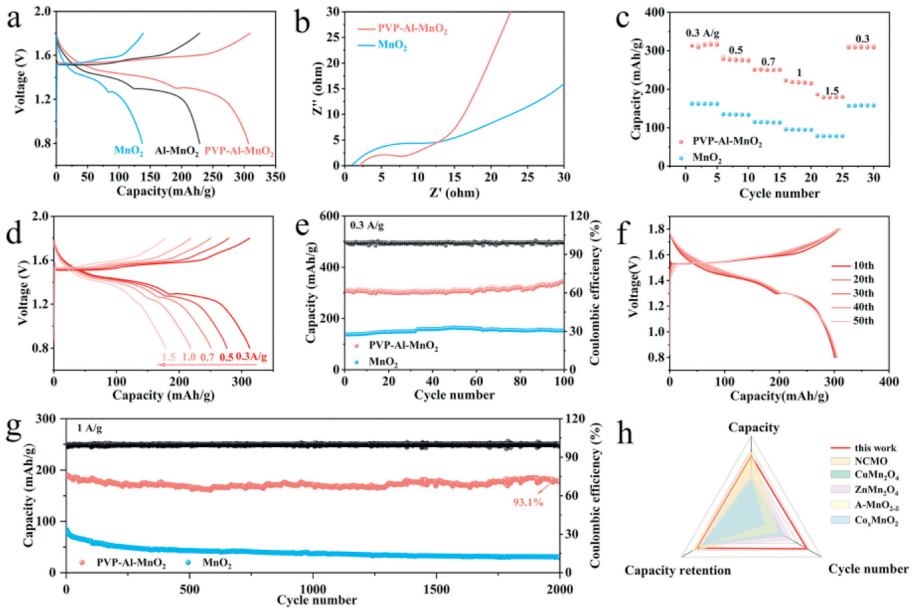


Fig. 3. Electrochemical performances of PVP-Al-MnO_2. (a) Charge/discharge profiles. (b) EIS spectra. (c) Rate performances. (d) Charge/discharge curves of PVP-Al-MnO_2. (e) Cycling behaviors of α-MnO_2 and PVP-Al-MnO_2. (f) Charge/discharge profiles at different cycles. (g) Cycle performance of PVP-Al-MnO_2 at 1.0 A/g. (h) Comparison of PVP-Al-MnO_2 and other cathodes.

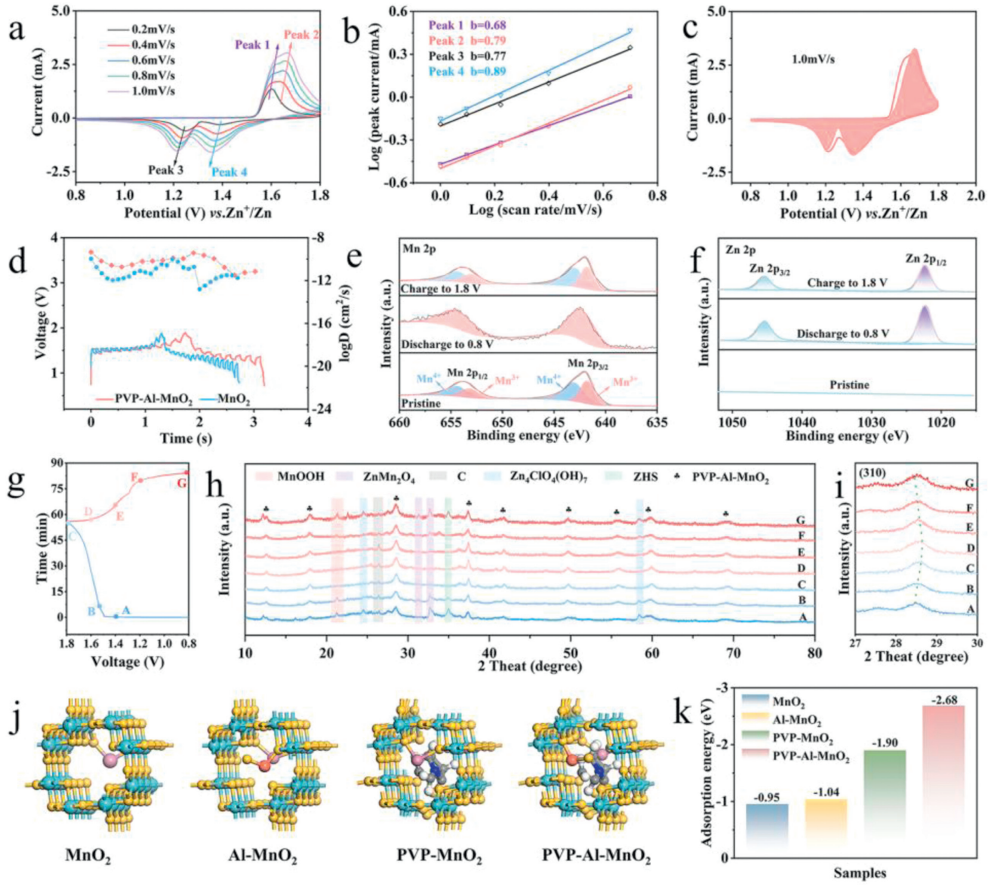


Fig. 4. Charge/discharge mechanism of PVP-Al-MnO_2. (a) CV profiles of PVP-Al-MnO_2 cathode. (b) The *b* value according to log*v* and log*i* plots. (c) CV curve with the capacitive-like portion. (d) GITT distributions and the corresponding ion diffusion coefficients of PVP-Al-MnO_2 cathode. XPS spectra of (e) Mn 2p and (f) Zn 2p. (g-i) *Ex-situ* XRD patterns. (j, k) Theoretical simulations, structural models and relative adsorption energy (E_{ads}) of Zn-ions absorbed.

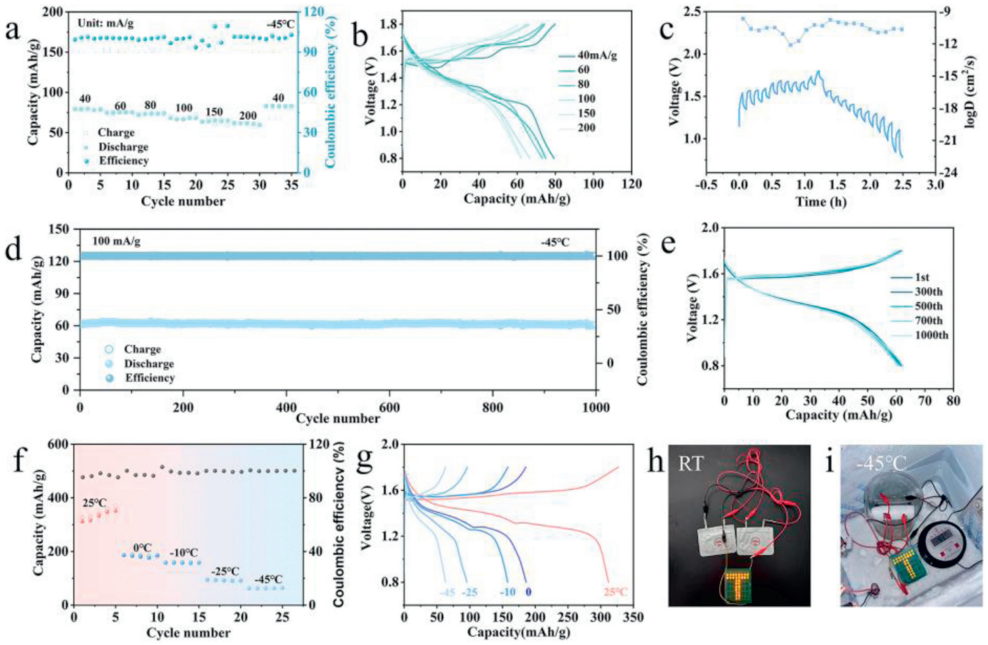


Fig. 5. Low-temperature electrochemical behaviors of PVP-Al-MnO_2. (a) Rate capacities and (b) the charge-discharge curves. (c) GITT curves and ion diffusion coefficients of PVP-Al-MnO_2 cathode. (d) Cycling behaviors at 100 mA/g and (e) the charge-discharge curves. (f) Electrochemical performances at various temperatures and (g) the corresponding charge-discharge profiles. The LED lights powered (h) at room temperature and (i) -45 °C.

63.1 % to 89.3 % with the increased scan rate, manifesting that the pseudocapacitance-controlled behavior is favorable for the high-rate behaviors.

The GITT were further conducted to evaluate the Zn^{2+} diffusion kinetics within the material (Fig. 4d). The Zn^{2+} diffusion coefficient can be estimated by the equation [54]:

$$D_{Zn}^{2+} = (4/\pi\tau)(m_B V_M / M_B A)^2 (\Delta E_s / \Delta E_\tau)^2 \quad (4)$$

where $D_{Zn^{2+}}$ is the diffusion coefficient of Zn^{2+}, τ is the pulse time, m_B and M_B are the molecular weight/mass of the active substance, V_M is the molar volume, A is the area, and $\Delta E_s/\Delta E_\tau$ is the steady-state voltage/total change of the battery voltage E. The $D_{Zn^{2+}}$ value of PVP-Al-MnO_2 estimated is $\sim 10^{-9}$ cm^2/s, which is noticeably higher than α-MnO_2 (Fig. 4d). This interprets why PVP-Al-MnO_2 exhibits improved rate performance and electrochemical stability compared with MnO_2 (Fig. 4d).

The charge compensation mechanism of PVP-Al-MnO_2 in the electrochemical processes was further explored by XPS measurements. The Mn 2p spectra of PVP-Al-MnO_2 show the variation of manganese valence during the discharge-charge process (Fig. 4e). When the material was discharged to 0.8 V, the ratio of Mn^{3+} is apparently increased in the Mn 2p spectra, proving that Mn^{4+} is partially decreased to Mn^{3+} ($2MnO_2 + Zn^{2+} + 2e^- \leftrightarrow ZnMn_2O_4$). When the battery was recharged to 1.8 V, the peak proportion of Mn^{4+} is increased prominently, implying that the extraction of zinc ions from the electrode is followed by the decline of Mn ions. The reversible valence variation of Mn 2p further proves the reversible charge storage in the PVP-Al-MnO_2 material. In addition, 2 peaks with binding energies of 1045.4 (Zn $2p_{3/2}$) and 1022.4 eV (Zn $2p_{1/2}$) are observed at fully charged and discharged states in the Zn 2p (Fig. 4f). This confirms the insertion of zinc ions into PVP-Al-MnO_2 framework in the discharge process. When the cell was charged to 1.8 V, Zn^{2+} cannot be fully extracted from the structure and there is some remaining Zn in the lattice.

The electrochemical energy storage mechanism for PVP-Al-MnO_2 was explored by *ex-situ* XRD results. The batteries with PVP-Al-MnO_2 cathodes, zinc anode and 3 mol/L $Zn(ClO_4)_2$/0.2 mol/L $MnSO_4$ electrolyte were cycled at 0.3 A/g, and the PVP-Al-MnO_2 electrodes were detached at different stages from A to G (Fig. 4g). The tunnel structure of PVP-Al-MnO_2 is well maintained in the whole electrochemical processes. From *ex-situ* XRD diffraction patterns (Fig. 4h), the formation of MnOOH (JPCDS No. 24-0713), $ZnMn_2O_4$ (JPCDS No. 71-2499), $Zn_4SO_4(OH)_6{\cdot}0.5H_2O$ (ZHS, JPCDS No. 44-0674), and $Zn_4ClO_4(OH)_7$ (PDF #41-0715) were simultaneously detected in the complete discharge product (G), consistent with previous results [55,56]. This suggests the electrochemical reaction mechanism of zinc ion and hydrogen ion intercalation into the PVP-Al-MnO_2 framework, which induces the generation of $ZnMn_2O_4$ and the formation of by-product hydroxides [57]. The products gradually disappear and regenerate in the charge and discharge processes, implying the reversible electrochemical reaction based on Zn^{2+} and H^+ ions intercalation/de-intercalation. Fig. 4i shows the variation of the (310) peaks in the electrochemical processes. The characteristic peaks shift to the lower angle during the discharge process and shift back to the higher angle during the charging process. This implies that the reversible intercalation/de-intercalation of Zn^{2+}/H^+ ions leads to the shift of the characteristic peaks. This strongly confirms that the introduction of PVP molecule and Al ions into α-MnO_2 does not change the structural characteristics of tunnel structure in the electrochemical reaction, although the electrochemical performances of the material are effectively enhanced. The Zn storage abilities of different materials were evaluated by calculating the E_{ads} of tunnel MnO_2 with various intercalations. As shown in Figs. 4j and k, the E_{ads} of Zn on Al and PVP co-intercalated MnO_2 shows lower E_{ads} than the unmodified MnO_2, Al-MnO_2 or PVP-intercalated MnO_2, indicating that the co-intercalation of Al and PVP into the tunnel material plays a synergetic role in enhancing the adsorption capability of Zn^{2+}. This could explain why the PVP-Al-MnO_2 material exhibits significantly enhanced capacity and long-life cycling stability (Fig. 3).

One of main technical challenges for aqueous battery systems is their poor low-temperature electrochemical performances, because the high liquid-solid transition temperature of aqueous electrolyte seriously limits the ion diffusion at low operation temperature. The 3 mol/L $Zn(ClO_4)_2$/0.2 mol/L $MnSO_4$ electrolyte is selected in this work. The Zn^{2+} storage capabilities of PVP-Al-MnO_2

electrode are therefore tested at a low working temperature of -45 °C (Fig. 5). The rate capabilities of PVP-Al-MnO_2 electrode and charge-discharge profiles are shown in Figs. 5a and b. It can be observed that the PVP-Al-MnO_2 electrode exhibits specific capacities of 79.9, 75.0, 73.5, 66.5, 65.3 and 60.9 mAh/g at 40, 60, 80, 100, 150 and 200 mA/g, respectively. The reversible capacity is restored to the original value when the current density is reduced to 40 mA/g, demonstrating the extremely high structural stability upon fast Zn^{2+} ion de(intercalation) processes on PVP-Al-MnO_2. The GITT measurement was also carried out to obtain the information on diffusion coefficient of PVP-Al-MnO_2 at -45 °C. The material shows an ion diffusion coefficient of 10^{-12}-10^{-9} cm^2/s at -45 °C, lower than the value at room temperature (Fig. 5c). The result confirms the low diffusion activity of PVP-Al-MnO_2 at -45 °C.

Figs. 5d and e depict the cycling behaviors of the PVP-Al-MnO_2 electrode and the charge-discharge profiles at 100 mA/g at -45 °C. The PVP-Al-MnO_2 electrode displays a capacity of 60.5 mAh/g at 100 mA/g with capacity retention of 98 % after 1000 cycles (Fig. 5d). Furthermore, the charge-discharge curves at 0.1 A/g (Fig. 5e) also displays similar electrochemical curves, confirming the outstanding electrochemical reversibility and structural stability of PVP-Al-MnO_2 electrode at -45 °C. The electrochemical behaviors of PVP-Al-MnO_2 material at various temperatures were also systematically examined. The electrochemical behaviors are effectively inhibited as the operation temperature reduces gradually from 25 °C to -45 °C. As shown in Figs. 5f and g, the PVP-Al-MnO_2 material exhibits reversible capacities of 332.7, 186.1, 157.9, 94.4 and 62.7 mAh/g at room temperature, 0, -10, -20 and -45 °C at 100 mA/g. The pouch cells were also constructed in order to test if the battery can operate properly in practice (Figs. 5h and i). Two pouch cells in-series can power LED lights properly at room temperature (Fig. 5h). When the working temperature is reduced to -45 °C, the LED lights can still be working as normal (Fig. 5i), confirming the excellent electrochemical performances of zinc-ion batteries at low temperature. Overall, the PVP-Al-MnO_2||$ZnClO_4$||Zn full cell described in this work is able to be working at low temperature.

In summary, PVP-Al-MnO_2 was synthesized through a hydrothermal method. The inorganic Al^{3+} ions and organic polyvinylpyrrolidone (PVP) are successfully incorporated into the tunnel α-MnO_2 structure. Structural characterizations (XRD, FTIR, Raman and XPS) confirm the incorporation of Al^{3+}/PVP into the tunnel α-MnO_2 structure, which leads to the distortion of MnO_6 octahedral framework. DFT calculations were conducted and the result reveals that the Zn^{2+} adsorption energy in the Al^{3+}/PVP co-intercalated material is effectively lowered when compared with the original α-MnO_2 structure. Electrochemical tests indicate that the PVP-Al-MnO_2 electrode exhibits excellent electrochemical performances, a reversible capacity of 306.8 mAh/g at 0.3 A/g and 93.1 % capacity retention over 2000 cycles at 1.0 A/g. Moreover, the aqueous PVP-Al-MnO_2||$ZnClO_4$||Zn battery can be working at low temperature (-45 °C). This work serves an encouraging approach to the modification and optimization of electrode materials for aqueous multivalent ion cells.

Declaration of competing interests

The authors declare that they have no known competing financial interests or personal relationships that could have appeared to influence the work reported in this paper.

CRediT authorship contribution statement

Mengdan Tian: Investigation. **Chuanzheng Zhu:** Investigation. **Kun Luo:** Supervision.

Supplementary materials

Supplementary material associated with this article can be found, in the online version, at doi:10.1016/j.cclet.2024.110702.

References

[1] S. Huo, L. Sheng, W. Xue, et al., Adv. Energy Mater. 13 (2023) 2204343.
[2] Y. Huang, J. Li, Adv. Energy Mater. 12 (2022) 2202197.
[3] T. Liu, A. Dai, J. Lu, et al., Nat. Commun. 10 (2019) 4721.
[4] J. Shin, D.S. Choi, H.J. Lee, et al., Adv. Energy Mater. 9 (2019) 1900083.
[5] G. Zhao, Y. Xing, Y. Liu, et al., Mater. Today Chem. 34 (2023) 101758.
[6] X. Zhang, C. Wang, J. Huang, et al., Angew. Chem. Int. Ed. 63 (2024) e202411884.
[7] B. Tang, L. Shan, S. Liang, et al., Energy Environ. Sci. 12 (2019) 3288–3304.
[8] S.Chen Ma, C. Long, et al., Adv. Energy Mater. 9 (2019) 1902446.
[9] X. Chen, W. Li, Z. Zeng, et al., Chem. Eng. J. 405 (2021) 126969.
[10] S. Wang, Z. Yang, B. Chen, et al., Energy Stor. Mater. 47 (2022) 491–499.
[11] S. Wang, Y. Ru, Y. Sun, et al., Chin. Chem. Lett. 34 (2023) 108143.
[12] C. Li, X. Zhang, G. Qu, et al., Adv. Energy Mater. 14 (2024) 2400872.
[13] C. Wang, X. Ji, J. Liang, et al., Angew. Chem. Int. Ed. 63 (2024) e202403187.
[14] T. Peng, Y. Xing, L. Mu, et al., Chin. Chem. Lett.36 (2025) 110039.
[15] Y. Zhu, W. Zhong, W. Chen, et al., Nano Energy 125 (2024) 109524.
[16] D. Chao, W. Zhou, C. Ye, et al., Angew. Chem. Int. Ed. 58 (2019) 7823–7828.
[17] G. Li, W. Chen, H. Zhang, et al., Adv. Energy Mater. 10 (2020) 1902085.
[18] S. Bi, S. Wang, F. Yue, et al., Nat. Commun. 12 (2021) 6991.
[19] C. Guo, R. Zhou, X. Liu, et al., Small 20 (2024) e2306237.
[20] Y. Liu, Z. Qin, X. Yang, et al., Energ. Stor. Mater. 56 (2023) 524–531.
[21] H. Li, H. Yao, X. Sun, et al., Chem. Eng. J. 446 (2022) 137205.
[22] L. Liu, Y.C. Wu, L. Huang, et al., Adv. Energy Mater. 11 (2021) 2101287.
[23] N. Subjalearndee, N. He, H. Cheng, et al., Adv. Fiber Mater. 4 (2022) 457–474.
[24] N. Li, Z. Hou, S. Liang, et al., Chem. Eng. J. 452 (2023) 139408.
[25] N. Zhang, X. Chen, M. Yu, et al., Chem. Soc. Rev. 49 (2020) 4203–4219.
[26] R. Zhao, C. Liu, Y. Zhu, et al., Adv. Funct. Mater. 34 (2024) 2316643.
[27] K.W. Nam, H. Kim, J.H. Choi, et al., Energy Environ. Sci. 12 (2019) 1999–2009.
[28] Y. Li, X. Liu, J T, et al., Chin. Chem. Lett. 36 (2025) 109551.
[29] T. Xiong, Z.G. Yu, H. Wu, et al., Adv. Energy Mater. 9 (2019) 1803815.
[30] X. Zhao, F. Zhang, H. Li, et al., Energy Environ. Sci. 17 (2024) 3629–3640.
[31] Q. Chen, X. Lou, Y. Yuan, et al., Adv. Mater. 35 (2023) e2306294.
[32] Y. Ma, M. Xu, R. Liu, et al., Energy Stor. Mater. 48 (2022) 212–222.
[33] R.Zhao Zhang, Y. Wang, et al., Angew. Chem. Int. Ed. 62 (2023) e202313163.
[34] Y. Zhao, R. Zhou, Z. Song, et al., Angew. Chem. Int. Ed. 61 (2022) e202212231.
[35] J. Huang, Z. Wang, M. Hou, et al., Nat. Commun. 9 (2018) 2906.
[36] S. Zhao, S. Wang, J. Guo, et al., Adv. Funct. Mater. 33 (2023) 2305700.
[37] Q. Zong, Y. Zhuang, C. Liu, et al., Adv. Energy Mater. 13 (2023) 2301480.
[38] X. Shan, F. Guo, K. Page, et al., Chem. Mater. 31 (2019) 8774–8786.
[39] H. Yao, H. Yu, Y. Zheng, et al., Angew. Chem. Int. Ed. 62 (2023) e202315257.
[40] M. Liu, J. Liu, B. Chen, et al., Small 18 (2022) e2105193.
[41] G. Chen, X. Zhou, Y. Bai, et al., Nano Energy 56 (2019) 884–892.
[42] S. Ding, X. Dai, Z. Li, et al., Energ. Stor. Mater. 47 (2022) 211–222.
[43] C. Chen, M. Shi, Y. Zhao, et al., Chem. Eng. J. 422 (2021) 130375.
[44] Z. Fu, D. Wang, Y. Yao, et al., Small 19 (2023) e2205666.
[45] R.Gao Zhang, L. Hu, et al., Chem. Eng. J. 417 (2021) 129186.
[46] X. Li, D. He, Q. Zhou, et al., Energy Environ. Sci. 17 (2024) 9195–9204.
[47] Y. Cai, R. Chua, S. Huang, et al., Chem. Eng. J. 396 (2020) 125221.
[48] S. Deng, Z. Tie, F. Yue, et al., Angew. Chem. Int. Ed. 61 (2022) e202115877.
[49] Y. Sun, Y. Liu, Z. Wang, et al., Chem. Eng. J. 484 (2024) 149573.
[50] K. Ma, S. Ge, R. Fu, et al., Chem. Eng. J. 484 (2024) 149525.
[51] S. Wang, Z. Yuan, X. Zhang, et al., Angew. Chem. Int. Ed. 60 (2021) 7056–7060.
[52] D. Wang, L. Wang, G. Liang, et al., ACS Nano 13 (2019) 10643–10652.
[53] N. Liu, X. Wu, L. Fan, et al., Adv. Mater. 32 (2020) e1908420.
[54] Y. An, Y. Tian, C. Liu, et al., ACS Nano 15 (2021) 15259–15273.
[55] X. Shen, X. Wang, Y. Zhou, et al., Adv. Funct. Mater. 31 (2021) 2101579.
[56] T. Sun, W. Zhang, Q. Nian, et al., Nanomicro. Lett. 15 (2023) 36.
[57] Q. Li, C. Wang, Y. Zhu, et al., Chem. Eng. J. 485 (2024) 150077.